SCIENTIFIC REPORTS
nature research

Check for updates

OPEN

Highly nonlinear magnetoelectric effect in buckled-honeycomb antiferromagnetic $Co_4Ta_2O_9$

Nara Lee[1,5], Dong Gun Oh[1,5], Sungkyun Choi[2,3], Jae Young Moon[1], Jong Hyuk Kim[1], Hyun Jun Shin[1], Kwanghyo Son[4], Jürgen Nuss[2], Valery Kiryukhin[3] & Young Jai Choi[1]✉

Strongly correlated materials with multiple order parameters provide unique insights into the fundamental interactions in condensed matter systems and present opportunities for innovative technological applications. A class of antiferromagnetic honeycomb lattices compounds, $A_4B_2O_9$ (A = Co, Fe, Mn; B = Nb, Ta), have been explored owing to the occurrence of linear magnetoelectricity. From our investigation of magnetoelectricity on single crystalline $Co_4Ta_2O_9$, we discovered strongly nonlinear and antisymmetric magnetoelectric behavior above the spin-flop transition for magnetic fields applied along two orthogonal in-plane directions. This observation suggests that two types of inequivalent Co^{2+} sublattices generate magnetic-field-dependent ferroelectric polarization with opposite signs. The results motivate fundamental and applied research on the intriguing magnetoelectric characteristics of these buckled-honeycomb lattice materials.

The emergence of novel cross-coupling effects generated by multiple order parameters in a wide range of materials has provided new perspectives into the interactions that occur in condensed matter systems[1,2]. Prominent examples are magnetoelectric and multiferroic materials where the cross-coupling between electric and magnetic properties has driven intense research to explore fundamental mechanisms responsible for the intrinsic magnetoelectric effects[3–9]. The primary focus of research activity in this field has on the emergence of ferroelectricity from different types of exotic magnetic orders and its dependence on applied magnetic fields. Some studies have emphasized also the potential of these materials in applications such as magnetoelectric memory and sensors by engineering their cross-coupling effects[10–13]. Despite the fact that quite a few magnetoelectric or multiferroic materials are known to us, it is still desired to discover new materials with stronger magnetoelectric coupling for enhancing the feasibility of utilizing their functionalities in device applications.

Materials composed of two-dimensional honeycomb lattices have been investigated due to possible occurrence of intriguing physical phenomena such as quantum spin liquid state[14–16] and electronic state with Dirac-like linear dispersion[17–19]. The antiferromagnet of $Co_4Nb_2O_9$ has recently been in focus for its linear magnetoelectric behavior[6,7,20–22]. $Co_4Nb_2O_9$ crystallizes in a trigonal $P\bar{3}c1$ structure with two different types of honeycomb layers stacked alternately along the c axis. In the single crystalline $Co_4Nb_2O_9$, grown by a floating zone method[23], antiferromagnetic order sets in below $T_N \approx 27$ K, concurrently with a linear magnetoelectric effect in applied magnetic fields[24–26]. A magnetic structure was observed as lowered monoclinic symmetry[21] and the presence of off-diagonal elements in the magnetoelectric tensor suggests the formation of toroidal moments[27–29].

Further studies of the magnetoelectric effect in honeycomb lattices were done on the isostructural compound $Co_4Ta_2O_9$ (CTO)[6,30,31]. In CTO, the antiferromagnetic order emerges at $T_N \approx 20$ K, simultaneously with the appearance of a dielectric anomaly and a ferroelectric polarization in applied magnetic fields. Until now, it has been believed that below T_N, the ferroelectric polarization in CTO increases monotonously under increasing applied magnetic fields, similar to that in $Co_4Nb_2O_9$[20–22]. However, these studies were performed only on polycrystalline samples, in which the physical properties are averaged out over all spatial directions due to a large number of grains of varying orientations. To overcome this challenge, we grew single crystals of CTO by utilizing the conventional flux method[32]. Despite an antiferromagnetic order of CTO on buckled-honeycomb

[1]Department of Physics, Yonsei University, Seoul 03722, Korea. [2]Max Planck Institute for Solid State Research, Heisenbergstrasse 1, 70569 Stuttgart, Germany. [3]Department of Physics and Astronomy, Rutgers University, Piscataway, NJ 08854, USA. [4]Department of Modern Magnetic Systems, Max Planck Institute for Intelligent Systems, Heisenbergstrasse 3, 70569 Stuttgart, Germany. [5]These authors contributed equally: Nara Lee and Dong Gun Oh. ✉email: phylove@yonsei.ac.kr

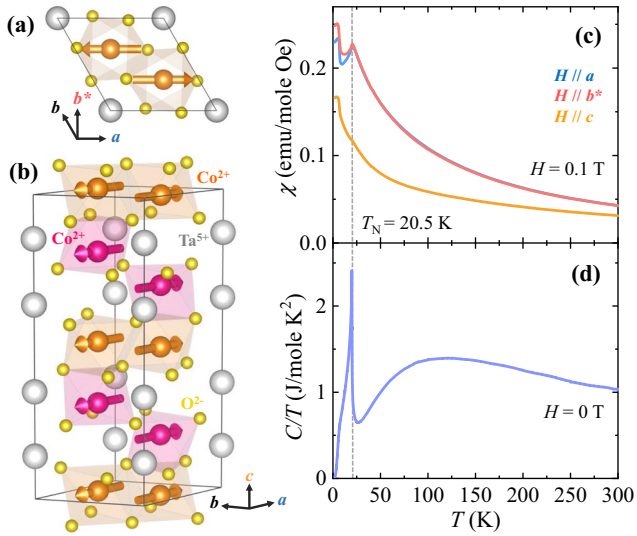

Figure 1. Crystallographic structure and temperature (T) dependence of magnetic properties. (**a**,**b**) Views of the crystal structure of $Co_4Ta_2O_9$ (a space group $P\bar{3}c1$, No. 165) with the Co^{2+} moments in a selected magnetic domain from the top (**a**) and the side (**b**). Orange and pink spheres with arrows represent two inequivalent Co^{2+} ions and their spin directions, and light grey and yellow spheres denote nonmagnetic Ta^{5+} and O^{2-} ions, respectively. The grey box with the rhombic cross-section represents the crystallographic unit cell. (**c**) T dependence of magnetic susceptibility, $\chi = M/H$, at magnetic field $H = 0.1$ T applied along the three inequivalent crystallographic orientations a, b^* and c. (**d**) T dependence of specific heat divided by the temperature, C/T, measured at $H = 0$ T. A dashed grey line indicates the Néel temperature, $T_N = 20.5$ K.

lattices, similar to the magnetic structure of $Co_4Nb_2O_9$[21], the single crystalline CTO reveals strongly nonlinear magnetoelectric effect which is unique among $A_4B_2O_9$ (A = Co, Fe, Mn and B = Nb, Ta) compounds[20,30,33–36]. This suggests the existence of two different polarization components originating from inequivalent Co^{2+} sublattices. Our nontrivial discovery calls for further experimental and theoretical studies to reveal the underlying microscopic mechanism.

Results and discussion

CTO crystallizes in a trigonal $P\bar{3}c1$ structure with unit cell dimensions of $a = 0.517$ nm, and $c = 1.413$ nm, obtained from the single crystal X-ray diffraction experiment (see Supplementary Information S1 for details). The crystallographic structures viewed from the top and side are depicted in Fig. 1a,b, respectively. Two dissimilar types of honeycomb layers are stacked alternatingly along the c axis. One layer consists of six edge-shared CoO_6 octahedra in the same plane, while the other consists of corner-shared octahedra buckled in a zig-zag arrangement around the ring[20]. Recent neutron diffraction measurements on single crystals of CTO[37] reveal a consistent result with the magnetic order shown in Fig. 1a,b when assuming a collinear arrangement of Co^{2+} moments. Considering the centrosymmetric trigonal structure with three-fold rotational symmetry about the c axis combined with two types of 180°-oriented antiferromagnetic domains leads to the possible formation of six types of 60°-oriented antiferromagnetic domains.

To examine the magnetic properties of CTO, the T dependence of the magnetic susceptibility, $\chi = M/H$, was measured at $H = 0.1$ T upon warming after zero-field-cooling. The anisotropic χ, obtained for the H along the three distinguishable axes a, b^*, and c, are shown in Fig. 1c. For the two orthogonal in-plane orientations, a and b^*, the χ exhibits a sharp anomaly at $T_N \approx 20.5$ K, indicating the emergence of antiferromagnetic order. The T dependence of C/T measured at zero H also shows a distinct anomaly at T_N (Fig. 1d). Above T_N, the χ for the two in-plane orientations decreases smoothly with T with nearly identical shapes. On the other hand, a weak anomaly at T_N is observed in the χ for the c axis.

The overall T dependence of χ, compared between in-plane and out-of-plane orientations, shows strong magnetic anisotropy, suggesting the in-plane antiferromagnetic alignment of Co^{2+} spins. The shape of χ curve for a and b^* axes are different below T_N and the faster decrease of χ for the a axis upon lowering T is observed because the spins in two types of the antiferromagnetic domains align along this axis. As T is further decreased, a sudden increase of χ occurs at $T_C = 6.5$ K. The characteristics of this transition were investigated in detail by AC χ measurement, which indicates the formation of a new phase such as a weakly ferromagnetic or/and glass state (see Supplementary Information S2 for details).

The isothermal M for the three inequivalent orientations was measured up to ± 9 T at $T = 2$ K, as shown in Fig. 2a. The M along the a direction (M_a) shows a broad bending at a low H regime. Upon increasing H further, the M_a increases monotonously and reaches 3.7 μ_B/f.u. at 9 T. The M_{b^*} exhibits a similar H dependence to the M_a; however, the magnetic moment at 9 T is found to be ~ 3.9 μ_B/f.u., which is slightly larger than that of the M_a. As manifested as the change in slope shown in the magnified plot of the M_a (Fig. 2b), the spin-flop transition occurs

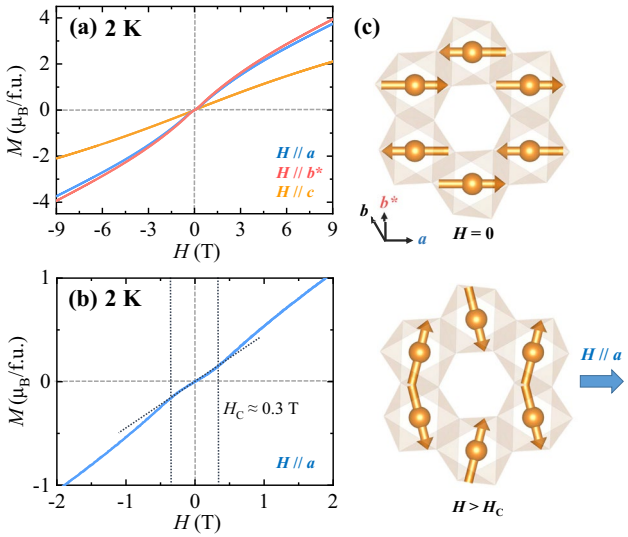

Figure 2. Anisotropic isothermal magnetization for $Co_4Ta_2O_9$. (**a**) Isothermal magnetization, M, measured at 2 K in the H range of ± 9 T along the a, b^* and c axes. (**b**) Magnified plot of M for the a direction. Short-dotted vertical lines indicate spin-flop transitions occurring at $H_C \approx \pm 0.3$ T. (**c**) Antiferromagnetic spin structure of Co^{2+} ions at $H = 0$ T (Top). Magnetic structure of Co^{2+} moments above the spin-flop transition, $H > H_C$ along the a axis (bottom).

at $H_C \approx 0.3$ T for an applied field along both a and b^* axes due to the angular distribution of antiferromagnetic domains. The spin structures below and above the spin-flop transition are displayed in Fig. 2c. Note that this result is different from the previous results on polycrystalline samples, where the spin-flop transition occurs at a higher H of ~ 0.9 T, possibly due to the averaging effect over grain orientations[31]. On the other hand, the M_c increases almost linearly up to 9 T resulting in a magnetic moment of ~ 2.1 μ_B/f.u. at 9 T, consistent with the strong magnetic anisotropy observed in the T dependence of anisotropic χ (Fig. 1c).

The anisotropic characteristics of magnetoelectric properties were examined through the T dependence of P for the a, b^*, and c axes. The magnitude of P was obtained by integrating the pyroelectric current density measured after poling in an electric field along the direction of P and H up to 9 T for the three different orientations, as shown in Fig. 3. Interestingly, the P emerges dominantly along the a axis below T_N (P_a, Fig. 3a–c) with an unusual T dependence upon increasing H. The other components of P do not vanish (P_{b^*} and P_c, Fig. 3d–i) similar to the T dependence of P in $Co_4Nb_2O_9$[21]. In detail, Fig. 3b shows the T-dependence of P_a at $H = 1$, 3, 5, 7, and 9 T along the b^* axis (H_{b^*}). The P_a at $H_{b^*} = 1$ T starts from a negative value of − 13.2 μC/m^2 at 2 K, increases monotonously to zero upon increasing T, and disappears at T_N. At $H_{b^*} = 3$ T, P_a exhibits the largest negative value of − 32.2 μC/m^2 at 2 K and crosses zero P_a at approximately 15 K. A similar trend of change in the sign of P_a is observed at $H_{b^*} = 5$ T with an upward shift in the overall magnitude of P_a. The P_a at $H_{b^*} = 7$ and 9 T retains positive values throughout the whole T range below T_N, and shows its maximum magnitude of 55.9 μC/m^2 at 2 K and $H_{b^*} = 9$ T. This strongly nonlinear magnetoelectric behavior is also observed in P_a at different values of H_a (Fig. 3a). At $H_a = 1$ T, the P_a is very small in magnitude and shows the negligible T dependence. The values of P_a at $H_a = 3$, 5, and 7 T are all negative at low temperatures. In contrast to the case of an in-plane H, the P_a under an applied H_c tends to increase gradually as H_c is increased, maintaining a positive value throughout the entire range of T below T_N (Fig. 3c). The P_a at $H_c = 9$ T and 2 K is found to be 78.7 μC/m^2 (Fig. 3c), which is approximately twice that of $P_a = 34.9$ μC/m^2 at $H_a = 9$ T and 2 K (Fig. 3a).

Figure 4a shows the T-dependence of dielectric constant for $E//a$ (ε_a'), measured at $H_{b^*} = 9$ T and $f = 100$ kHz. The ε_a' at 9 T exhibits a very sharp peak at 20.02 K with a 2.8% change in its magnitude (at the peak maximum). The sharpness of the peak at 9 T is characterized by the very small full width at half maximum (FWHM) estimated to be only 0.08 K, which indicates a good crystal quality. As H is decreased, the peak of ε_a' shifts progressively to a higher T with a gradual reduction of the peak height (Fig. 4b) and almost disappears at 4 T. At 5 T, a tiny peak in ε_a', with only 0.27% change in the overall magnitude, occurs at 20.37 K.

The nonlinear behavior of P and the intricate relationship between magnetic and electric properties in CTO were examined in detail by comparing the H dependence of P, M, and ε' at 2 K. The isothermal P_a was obtained by integrating the magnetoelectric current density, measured by sweeping the H_{b^*} between 9 and − 9 T at 2 K after poling in $H_{b^*} = 9$ T and $E_a = 4.72$ kV/cm, as shown in Fig. 5a. Starting from the maximum value of $P_a = 52.5$ μC/m^2 at 9 T, the P_a decreases upon decreasing H_{b^*} and becomes zero at 6.3 T. As H_{b^*} is decreased further, the P_a shows a broad minimum at 3.2 T with $P_a = -27.5$ μC/m^2. Below $H_C \approx 0.3$ T, P_a disappears. Further decrease in H in the negative direction leads to the antisymmetric H dependence of the P_a. The sweeping of H_{b^*} from − 9 to + 9 T completes the isothermal P_a curve, showing negligible magnetic hysteresis. In Fig. 5b, the magnetodielectric (MD) effect, described by the variation of ε_a' by applying H_{b^*} and defined as MD_a (%) $= \frac{\varepsilon'(H) - \varepsilon'(0T)}{\varepsilon'(0T)} \times 100$, was measured up to ± 9 T at $f = 100$ kHz and $T = 2$ K. The initial curve of MD_a exhibits a slight curvature at low H_{b^*} regime and the maximum slope at $H_C \approx 0.3$ T. Above H_C, the MD_a reduces more gradually which becomes almost

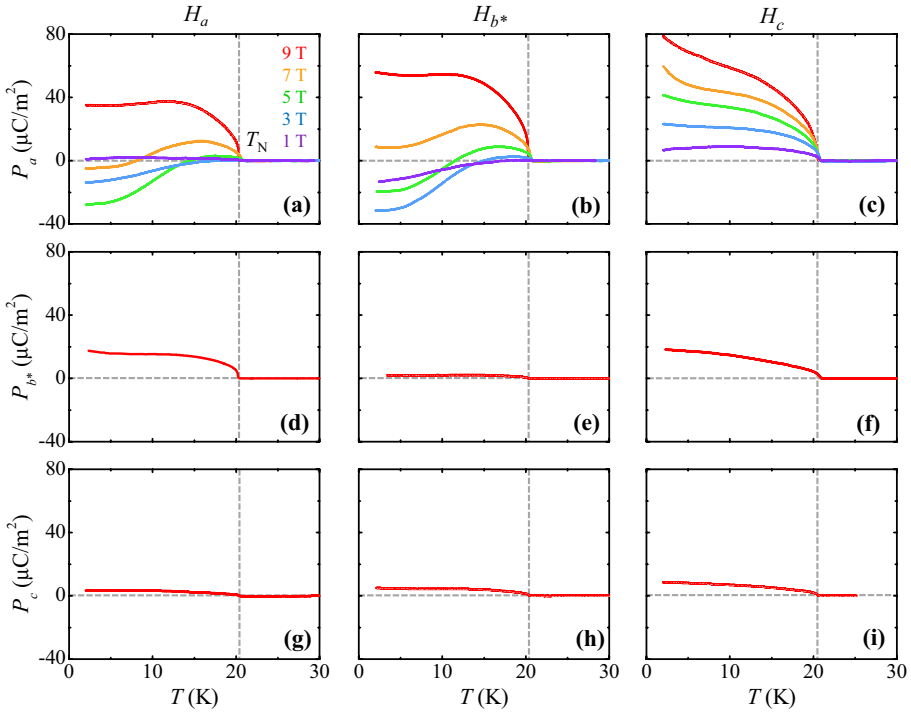

Figure 3. Temperature dependence of the anisotropic ferroelectric polarization. (**a**–**c**) T dependence of P_a obtained by integrating the pyroelectric current after poling from 100 to 2 K in at H_a, H_{b*}, and H_c, respectively. P_a was measured at $H = 1$, 3, 5, 7 and 9 T. (**d**–**f**) T dependence of P_{b*} measured at $H_a = 9$ T, H_{b*}, and H_c, respectively. (**g**–**i**) T dependence of P_c measured at $H_a = 9$ T, H_{b*}, and H_c, respectively.

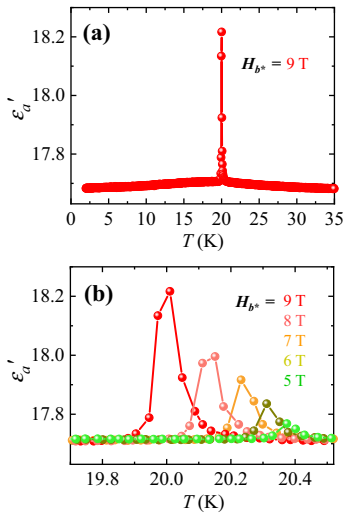

Figure 4. Dielectric constant along the a axis at H_{b*} with $f = 100$ kHz. (**a**) T dependence of dielectric constant, ε_a', below 35 K at $H_{b*} = 9$ T. (**b**) T dependence of ε_a' in a narrow range of T near T_N at $H_{b*} = 5$, 6, 7, 8, and 9 T.

linear above $H_{b*} = 1.5$ T. The maximum variation of MD_a is found to be approximately −0.36% at 9 T. The full MD_a curve appears to be symmetric because the direction of P_a is indistinguishable in the AC excitation of E_a for the ε_a' measurement. For a precise comparison with the MD_a, the H_{b*} derivative of isothermal M_{b*}, dM_{b*}/dH_{b*} at 2 K is also plotted in Fig. 5c. The dM_{b*}/dH_{b*} increases linearly up to H_C and reveals a kink at H_C, after which it begins to decrease. To elucidate the H_a and H_c dependences of P_a (Fig. 3a,c), the detailed field dependent behaviors as Fig. 5 are also included in the Supplementary Information S3.

The T evolution of strongly nonlinear magnetoelectric effect in CTO is presented, which shows that the major features are preserved at 10 K above $T_C = 6.5$ K. Figure 6 shows the comparison among isothermal P_a, M_{b*}, and dM_{b*}/dH_{b*} at M_{b*} up to ± 9 T and $T = 5$, 10, 15, and 20 K below T_N. At 5 K, the overall H_{b*} dependences of P_a and

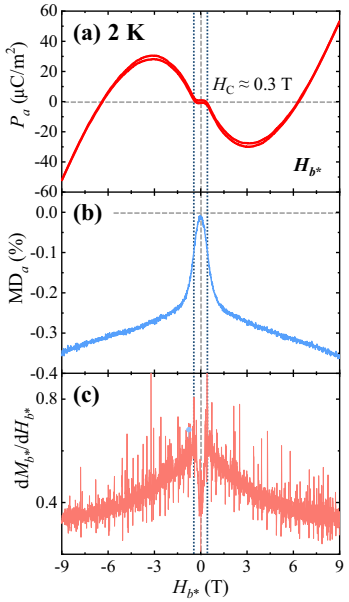

Figure 5. Comparison of electric and magnetic properties. (**a**) H_{b^*} dependence of P_a at $T = 2$ K. (**b**) H_{b^*} dependence of the magnetodielectric effect along the a axis, MD_a (%) $= \frac{\varepsilon'(H)-\varepsilon'(0\mathrm{T})}{\varepsilon'(0\mathrm{T})} \times 100$, measured with AC excitation of $E_a = 1$ V at $f = 100$ kHz and $T = 2$ K. (**c**) H_{b^*} derivative of M_{b^*} at 2 K.

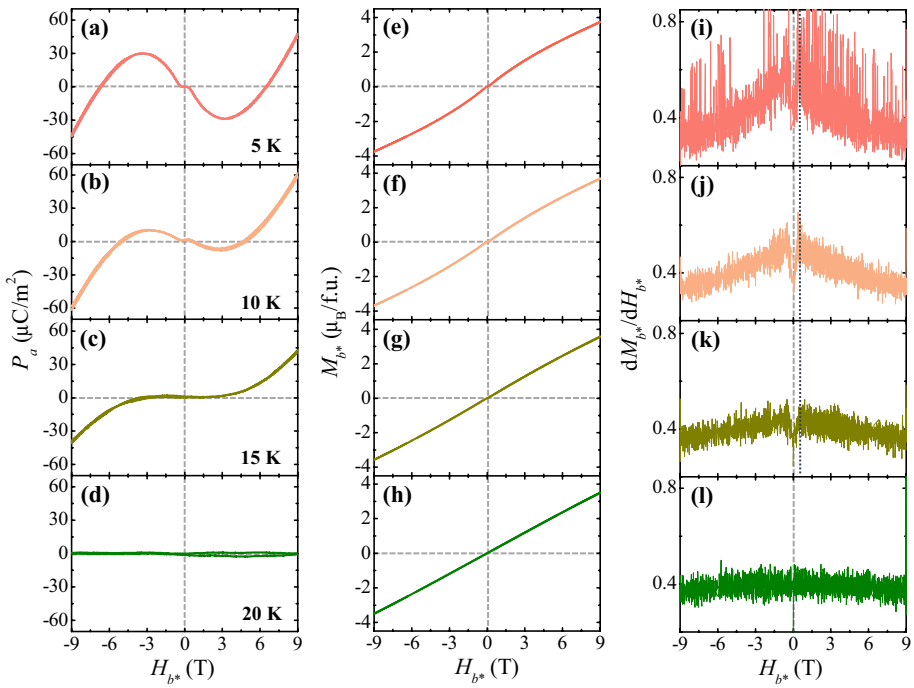

Figure 6. Temperature evolution of ferroelectric polarization and magnetization. (**a**–**d**) H_{b^*} dependence of ferroelectric polarization (P_a) at $T = 5$, 10, 15 and 20 K, respectively, obtained by integrating the magnetoelectric current measured changing H_{b^*} at the rate of 0.01 T/s up to ± 9 T after poling in $E_a = 4.72$ kV/cm and $H_{b^*} = 9$ T. (**e**–**h**) H_{b^*} dependence of magnetization (M_{b^*}) at $T = 5$, 10, 15 and 20 K, respectively, measured up to ± 9 T. (**i**–**l**) H_{b^*} derivative of M_{b^*} at $T = 5$, 10, 15 and 20 K, respectively.

M_{b^*} tend to behave akin to those at 2 K (Figs. 2a, 5a). In comparison with the P_a at 2 K, the maximum value of P_a at 5 K and 9 T reduces slightly to 45.1 μC/m^2 (Fig. 6a) and the M_{b^*} at 9 T also decreases to ~ 3.72 μ_B/f.u. (Fig. 6e). Upon decreasing H_{b^*}, a broad minimum of the P_a (= − 31.8 μC/m^2) occurs at 3.1 T (Fig. 6a) and the dM_{b^*}/dH_{b^*} at 5 K reveals kinks at H_C = ± 0.3 T (Fig. 6i), consistent with the plateau region within H_C in the P_a curve (Fig. 6a). At 10 K, the broad minimum of P_a occurs at 2.9 T with a significantly reduced value of − 8.1 μC/m^2 (Fig. 6b). However, the maximum value of P_a = 58.9 μC/m^2 at 9 T is found to be the largest despite the slight decrease of M^{b^*} (~ 3.64 μ_B/f.u., Fig. 6f). At 15 K, the regime of nearly zero P_a extends up to ± 3.0 T with the absence of the broad minimum (Fig. 6c). At 20 K, the P_a almost disappears (Fig. 6d) throughout the measurement region of H_{b^*} while the M_{b^*} shows a linear increase upon increasing H_{b^*} and finally becomes ~ 3.50 μ_B/f.u. at 9 T (Fig. 6h).

Distinctive from the linear magnetoelectric behavior in the isostructural $Co_4Nb_2O_9$, the electric polarization in CTO arises at the spin-flop transition above which strongly nonlinear and antisymmetric field dependence was observed. The linear magnetoelectric response and controllable electric polarization by rotating magnetic fields[38] in $Co_4Nb_2O_9$ have recently been explained by several theoretical works such as the orbital model incorporating local spin–orbit coupling at the site of Co^{2+} ion[39] and symmetry interpretation considering local C_3 point group[40]. In such theoretical analyses, the contributions from two types of magnetic sublattices, which are associated with two dissimilar types of honeycomb layers, to the net electric polarization are not distinguishable. Another theoretical work based on the Hartree–Fock calculations presents a noticeable consequence that each magnetic sublattice produces electric polarization with a different magnitude and direction, each of which varies linearly with the applied magnetic field strength[6]. The superposition of two different contributions leads to a linear behavior in the total polarization. However, the highly-nonlinear magnetoelectric effect of our CTO in the P_a under H_a and H_{b^*} implies the more intricate contribution of each sublattice to the magnetic-field dependent polarization. In particular, above the spin-flop transition, the dominant negative-polarization arising from one sublattice gives rise to the negative net P_a, but the gradual increase of the positive-polarization from the other sublattice results in the broad minimum and further increase of the net P_a upon increasing the field. Therefore, our results motivate more elaborate theoretical calculations comprising other factors such as additional lattice and magnetic domain contributions, and possible change of magnetic structure driven by electric field poling, which have not been considered in the previous studies.

Conclusion

In summary, we have synthesized single crystals of magnetoelectric $Co_4Ta_2O_9$ and explored magnetic and magnetoelectric properties along different crystallographic orientations. Despite the presence of several off-diagonal components, the dominant magnetic-field-driven change of polarization occurs for the *a* axis. More importantly, an antiferromagnetic order below T_N = 20.5 K leads to a highly nonlinear magnetoelectric effect above the spin-flop transition for in-plane magnetic fields. This is clearly different from the linear magnetoelectricity in other isostructural compounds, and indicates the complex evolution of polarization components with opposite signs originating from two different Co^{2+} sublattices. Our results provide insights into fundamental magnetoelectric interactions in the family of the buckled-honeycomb magnetoelectric magnets, paving way for the discovery of novel materials for magnetoelectric functional applications.

Methods

Hexagonal plate-like single crystals of CTO were grown by the conventional flux method with NaF, Na_2CO_3, and V_2O_5 fluxes in air[32]. Co_3O_4, and Ta_2O_5 powders were mixed in the stoichiometric ratio and ground in a mortar, followed by pelletizing and calcining at 900 °C for 10 h in a box furnace. The calcined pellet was finely reground and sintered at 1,000 °C for 15 h. After regrinding, the same sintering procedure was carried out at 1,100 °C for 24 h. A mixture of pre-sintered polycrystalline powder and fluxes was heated to 1,280 °C in a Pt crucible. It was melted at the soaking *T*, slowly cooled to 800 °C at a rate of 1 °C/h, and cooled to room *T* at a rate of 100 °C/h.

The temperature (*T*) and magnetic-field (*H*) dependences of the DC magnetization (*M*) were measured using a vibrating sample magnetometer at *T* = 2–300 K and *H* = − 9 to 9 T in a physical properties measurement system (PPMS, Quantum Design, Inc.). The specific heat (*C*) was measured with the standard relaxation method in the PPMS. The *T* and *H* dependences of dielectric constant (*ε'*) were observed at *f* = 100 kHz using an LCR meter (E4980, Agilent). The *T* and *H* dependences of electric polarization (*P*) was obtained by integrating pyro- and magneto-electric currents, respectively, measured after poling in a static electric field (*E*).

Received: 29 May 2020; Accepted: 6 July 2020
Published online: 23 July 2020

References

1. Hill, N. A. Density functional studies of multiferroic magnetoelectrics. *Annu. Rev. Mater. Res.* **32**, 1–37 (2002).
2. Salje, E. & Devarajan, V. Phase transitions in systems with strain-induced coupling between two order parameters. *Phase Trans.* **6**, 235–247 (1986).
3. Eerenstein, W., Mathur, N. D. & Scott, J. F. Multiferroic and magnetoelectric materials. *Nature* **442**, 759–765 (2006).
4. Vaz, C. A. F., Hoffman, J., Ahn, C. H. & Ramesh, R. Magnetoelectric coupling effects in multiferroic complex oxide composite structures. *Adv. Mater.* **22**, 2900–2918 (2010).
5. Ederer, C. & Spaldin, N. A. Weak ferromagnetism and magnetoelectric coupling in bismuth ferrite. *Phys. Rev. B* **71**, 060401(R) (2005).
6. Solovyev, I. V. & Kolodiazhnyi, T. V. Origin of magnetoelectric effect in Co4Nb2O9 and Co4Ta2O9: The lessons learned from the comparison of first-principles-based theoretical models and experimental data. *Phys. Rev. B* **94**, 094427(R) (2016).
7. Deng, G. *et al.* Spin dynamics and magnetoelectric coupling mechanism of $Co_4Nb_2O_9$. *Phys. Rev. B* **97**, 085154(R) (2018).
8. Kimura, T. Magnetoelectric hexaferrites. *Annu. Rev. Condens. Matter Phys.* **3**, 93–110 (2012).

9. Choi, Y. J. *et al.* Thermally or magnetically induced polarization reversal in the Multiferroic $CoCr_2O_4$. *Phys. Rev. Lett.* **102**, 067601 (2009).
10. Scott, J. F. Multiferroic memories. *Nat. Mater.* **6**, 256–257 (2007).
11. Fusil, S., Garcia, V., Barthélémy, A. & Bibes, M. Magnetoelectric devices for spintronics. *Annu. Rev. Mater. Res.* **44**, 91–116 (2014).
12. Street, M. *et al.* Increasing the Néel temperature of magnetoelectric chromia for voltage-controlled spintronics. *Appl. Phys. Lett.* **104**, 222402 (2014).
13. Baek, S. H. *et al.* Ferroelastic switching for nanoscale non-volatile magnetoelectric devices. *Nat. Mater.* **9**, 309–314 (2010).
14. Han, T. H. *et al.* Fractionalized excitations in the spin-liquid state of a kagome-lattice antiferromagnet. *Nature* **492**, 406–410 (2012).
15. Banerjee, A. *et al.* Proximate Kitaev quantum spin liquid behaviour in a honeycomb magnet. *Nat. Mater.* **15**, 733 (2016).
16. Chaloupka, J., Jackeli, G. & Khaliullin, G. Kitaev-Heisenberg model on a honeycomb lattice: Possible exotic phases in iridium oxides A_2IrO_3. *Phys. Rev. Lett.* **105**, 027204 (2010).
17. Castro Neto, A. H., Guinea, F., Peres, N. M. R., Novoselov, K. S. & Geim, A. K. The electronic properties of graphene. *Rev. Mod. Phys.* **81**, 109–162 (2009).
18. Sato, T. *et al.* Direct evidence for the dirac-cone topological surface states in the ternary chalcogenide $TlBiSe_2$. *Phys. Rev. Lett.* **105**, 136802 (2010).
19. Zhang, H. *et al.* Topological insulators in Bi_2Se_3, Bi_2Te_3 and Sb_2Te_3 with a single Dirac cone on the surface. *Nat. Phys.* **5**, 438–442 (2009).
20. Fang, Y. *et al.* Large magnetoelectric coupling in $Co_4Nb_2O_9$. *Sci. Rep.* **4**, 3860 (2014).
21. Khanh, N. D. *et al.* Magnetoelectric coupling in the honeycomb antiferromagnet $Co_4Nb_2O_9$. *Phys. Rev. B* https://doi.org/10.1103/PhysRevB.93.075117 (2016).
22. Yin, L. H. *et al.* Colossal magnetodielectric effect and spin flop in magnetoelectric $Co_4Nb_2O_9$ crystal. *Appl. Phys. Lett.* **109**, 032905 (2016).
23. Cao, Y. *et al.* High-quality single crystal growth and spin flop of multiferroic $Co_4Nb_2O_9$. *J. Crystal Growth* **420**, 90–93 (2015).
24. Fiebig, M. Revival of the magnetoelectric effect. *J. Phys. D Appl. Phys.* **38**, R123–R152 (2005).
25. Dzyaloshinskii, I. E. On the magneto-electrical effect in antiferromagnets. *Sov. Phys. JETP* **10**, 628–629 (1959).
26. Astrov, D. N. The magnetoelectric effect in antiferromagnetics. *Sov. Phys. JETP* **11**, 708–709 (1960).
27. Gorbatsevich, A. A. & Kopaev, Y. V. Toroidal order in crystals. *Ferroelectrics* **161**, 321–334 (1994).
28. Spaldin, N. A., Fiebig, M. & Mostovoy, M. The toroidal moment in condensed-matter physics and its relation to the magnetoelectric effect. *J. Phys. Condens. Matter* **20**, 434203 (2008).
29. Popov, Y. F., Kadomtseva, A. M., Belov, D. V. & Vorob'ev, G. P. Magnetic-field-induced toroidal moment in the magnetoelectric Cr_2O_3. *JETP Lett.* **69**, 330–335 (1999).
30. Fang, Y. *et al.* Magnetic-field-induced dielectric anomaly and electric polarization in $Co_4Ta_2O_9$. *J. Am. Ceram. Soc.* **98**, 2005–2007 (2015).
31. Chaudhary, S., Srivastava, P., Kaushik, S. D., Siruguri, V. & Patnaik, S. Nature of magnetoelectric coupling in corundum antiferromagnet $Co_4Ta_2O_9$. *J. Magn. Magn. Mater.* **475**, 508–513 (2019).
32. Wanklyn, B. M., Wondre, F. R., Garrard, B. J., Smith, S. H. & Davidson, W. The flux growth of some new rare earth and iron group complex oxides. *J. Mater. Sci.* **13**, 89–96 (1978).
33. Narayanan, N. *et al.* Magnetic structure and spin correlations in magnetoelectric honeycomb $Mn_4Ta_2O_9$. *Phys. Rev. B* **98**, 134438 (2018).
34. Fang, Y. *et al.* Magnetic-field-induced dielectric anomaly and electric polarization in $Mn_4Nb_2O_9$. *J. Appl. Phys.* **117**, 17B712 (2015).
35. Maignan, A. & Martin, C. Type-II multiferroism and linear magnetoelectric coupling in the honeycomb $Fe_4Ta_2O_9$ antiferromagnet. *Phys. Rev. Mater.* **2**, 091401(R) (2018).
36. Maignan, A. & Martin, C. Fe4Nb2O9: A magnetoelectric antiferromagnet. *Phys. Rev. B* **97**, 161106(R) (2018).
37. Choi, S. *et al.* Noncollinear antiferromagnetic order in the buckled honeycomb lattice of magnetoelectric $Co_4Ta_2O_9$ determined by single-crystal neutron diffraction. arXiv:2007.06561 (2020).
38. Khanh, N., Abe, N., Kimura, S., Tokunaga, Y. & Arima, T. Manipulation of electric polarization with rotating magnetic field in a honeycomb antiferromagnet $Co_4Nb_2O_9$. *Appl. Phys. Lett.* **96**, 094434 (2017).
39. Yanagi, Y., Hayami, S. & Kusunose, H. Manipulating the magnetoelectric effect: Essence learned from $Co_4Nb_2O_9$. *Phys. Rev. B* **97**, 020404 (2018).
40. Matsumoto, M. & Koga, M. Symmetry analysis of magnetoelectric effects in honeycomb antiferromagnet $Co_4Nb_2O_9$. *J. Phys. Soc. Jpn.* **88**, 094704 (2019).

Acknowledgements

The work at Yonsei was supported by the National Research Foundation of Korea (NRF) Grants (NRF-2017R1A5A1014862 (SRC program: vdWMRC center), NRF-2018R1C1B6006859, and NRF-2019R1A2C2002601). VK and SC were supported by the NSF, Grant No DMR-1609935. SC was also supported by the international postdoctoral scholarship at Max Planck Institute for Solid State Research, Stuttgart, Germany. The authors are grateful to Prof. G. Schütz for supporting AC measurements with the MPMS magnetometry.

Author contributions

N.L. and Y.J.C. designed the experiments. D.G.O. and N.L. synthesized the single crystals. D.G.O., J.Y.M, J.H.K., H.J.S. and N.L. performed the magnetization, heat capacity, dielectric constant, and polarization measurements. J.N. did single crystal XRD measurements and J.N. and S.C. did the nuclear structure analysis. S.C., K.S. and V.K. performed AC magnetic susceptibility measurements and analysis. D.G.O., S.C., N.L. and Y.J.C. analyzed the data and prepared the manuscript. All the authors have read and approved the final version of the manuscript.

Competing interests

The authors declare no competing interests.

Additional information

Supplementary information is available for this paper at https://doi.org/10.1038/s41598-020-69117-5.

Correspondence and requests for materials should be addressed to Y.J.C.

Reprints and permissions information is available at www.nature.com/reprints.

Publisher's note Springer Nature remains neutral with regard to jurisdictional claims in published maps and institutional affiliations.

Open Access This article is licensed under a Creative Commons Attribution 4.0 International License, which permits use, sharing, adaptation, distribution and reproduction in any medium or format, as long as you give appropriate credit to the original author(s) and the source, provide a link to the Creative Commons license, and indicate if changes were made. The images or other third party material in this article are included in the article's Creative Commons license, unless indicated otherwise in a credit line to the material. If material is not included in the article's Creative Commons license and your intended use is not permitted by statutory regulation or exceeds the permitted use, you will need to obtain permission directly from the copyright holder. To view a copy of this license, visit http://creativecommons.org/licenses/by/4.0/.

© The Author(s) 2020